

Imaging the Freeze-out Source and Extracting Strong Interaction Parameters in Relativistic Heavy Ion Collisions

Junhuai Xu,^{1,*} Zhi Qin,^{1,†} Renjie Zou,¹ Dawei Si,¹ Sheng Xiao,¹ Baiting Tian,¹ Yijie Wang,^{1,‡} and Zhigang Xiao^{1,2,§}

¹*Department of Physics, Tsinghua University, Beijing 100084, China*

²*Center of High Energy Physics, Tsinghua University, Beijing 100084, China*

(Dated: December 23, 2024)

Combining the femtoscopy interferometry and the optical deblurring algorithm, we implement a novel method to image the source formed in heavy ion collisions (HICs), while the interaction strength between the particle pair can be determined simultaneously. By applying this method to Au+Au collisions at $\sqrt{S_{NN}} = 200$ GeV, the spatial distribution of the emission source has been reconstructed for protons (p) and antiprotons (\bar{p}) from the respective pp and $\bar{p}\bar{p}$ correlation functions. Within experimental uncertainties, protons and antiprotons share the same freeze-out distribution showing higher density in the center compared to the widely assumed Gaussian shape. The results evidence the matter-antimatter symmetry in coordinate space at the moment of freeze-out before the nucleons are fully randomized in the collisions.

I. INTRODUCTION

It is accepted that matter and antimatter are created in equal amount in the first moments after the Big Bang. Yet today, we observe a universe filled with matter far exceeding antimatter. This puzzling phenomenon is related to the profound symmetry breaking in nature and remains a challenge in nuclear and particle physics. On modern accelerators, heavy ion collisions (HICs) create conditions akin to those in the early universe. So after the success of observing the production of antimatter [1–3], people can further investigate the spatial evolution and decoupling of the matter and antimatter on the femtosopic scale.

The HBT intensity interferometry, invented by Hanbury-Brown and Twiss to detect the angular radius of Sirius [4], has been generalized and applied extensively in nuclear physics [5, 6] to extract the temporal-spatial feature of the emission source formed in HICs by measuring the emitted particle pair correlation function (CF) at small relative momentum. In a basic picture, the CF is the result of the low-energy scattering between the particle pair emitted from the source, and carries the information of the interaction strength, defined by the scattering length f_0 and effective range d_0 between the pair, written as (f_0, d_0) in short.

Thus, simultaneous inference of the source distribution and the interaction strength becomes feasible for either particle or antiparticle pairs. Based on the Lednický-Lyuboshitz (LL) model, STAR Collaboration has verified that protons and antiprotons exhibit nearly identical interaction properties, and the extracted source size parameters (Gaussian source) for pp and $\bar{p}\bar{p}$ pairs were found to be similar [7]. Specifically, within experimental

uncertainties, the parameters (f_0, d_0) are equivalent for pp and $\bar{p}\bar{p}$ pairs, consistent with CPT symmetry. The Gaussian source assumption has become widely adopted in correlation function analysis, from which significant results have been obtained in the studies of particle interactions and source distributions [8–11].

However, by Gaussian parameterization it is assumed that all the participants are totally randomized in space prior to the freeze-out instant, and the initial state as well as the evolution details of the colliding system are lost. This strong assumption is unfavorable in the context of various recent studies. For two examples, i) high energy HIC has been applied to infer the initial shape of the colliding nuclei [12, 13]. ii) The Ohm's law is suggestively broken because of the strong field and extremely short evolution time [14]. In both cases it is of importance to probe the spatial evolution of the colliding system. Thus, it is surely nontrivial to abandon the Gaussian assumption.

Despite of the difficulty in solving inverse problem, the direct imaging of the source has been achieved without introducing the analytic parameterization [15–17]. More recently, the Bayesian-based deblurring method, known as Richardson-Lucy (RL) algorithm [18, 19] which was initially developed for optical imaging [20], has gained prominence in nuclear physics [21–25]. Particularly, Nzabahimana et al. [22] applied the RL algorithm in source imaging in HICs, highlighting the method's effectiveness and robustness. In this letter, combining the RL deblurring algorithm and the LL model incorporating the pair interaction, we bring the realisation to solve the inverse problem of source imaging from the experimental CFs. The source distribution and (f_0, d_0) are determined simultaneously. The similarity of the source spatial distribution of p and \bar{p} formed in HICs has been demonstrated.

* xjh22@mails.tsinghua.edu.cn

† qinz18@mails.tsinghua.edu.cn

‡ yj-wang15@tsinghua.org.cn

§ xiaozg@tsinghua.edu.cn

II. METHOD DESCRIPTION

Defined as a function of the relative momentum $\mathbf{q} = \mathbf{p}_1 - \mathbf{p}_2$ in the particle pair rest frame (PRF), the CF is given experimentally by $C(\mathbf{q}) = \frac{P(\mathbf{p}_1, \mathbf{p}_2)}{P(\mathbf{p}_1)P(\mathbf{p}_2)}$, where $P(\mathbf{p}_1)$ and $P(\mathbf{p}_2)$ are the probabilities of detecting particles with momenta \mathbf{p}_1 and \mathbf{p}_2 , respectively, and $P(\mathbf{p}_1, \mathbf{p}_2)$ is the joint probability of detecting both particles simultaneously. For uncorrelated emissions, $C = 1$ is expected. Theoretically, the CF can be calculated using the Koonin-Pratt (KP) formula [26, 27]

$$C(\mathbf{q}) = \int d^3r |\Psi_{\mathbf{q}}(\mathbf{r}')|^2 S(\mathbf{r}) \quad (1)$$

where S is the source function (SF) related to the relative distance $\mathbf{r} = \mathbf{r}_1 - \mathbf{r}_2$ of the particle-pair in the source rest frame, and $\Psi_{\mathbf{q}}(\mathbf{r}')$ is the wave function calculated from the relative momentum \mathbf{q} and distance \mathbf{r}' in the PRF.

The LL model [28] provides a framework to describe the interaction strength between particle pairs through the parameters (f_0, d_0) , which characterize the S-wave scattering amplitude under the effective range approximation. The model assumes that higher-order correlations involving three or more particles are negligible, the electromagnetic effects generated by the source are insignificant, and the momentum transfer from final-state interactions is small enough to apply the smoothness approximation. Within this model, the relative wave function for pp and $\bar{p}\bar{p}$ pairs in the PRF is expressed as

$$\begin{aligned} \psi_{\mathbf{q}}(\mathbf{r}) = & e^{i\delta_c} \sqrt{A_c(\eta)} [e^{-i\frac{1}{2}\mathbf{q} \cdot \mathbf{r}} F(-i\eta, 1, i(\frac{1}{2}\mathbf{q} \cdot \mathbf{r} + \frac{1}{2}qr))] \\ & + f_c(q) \frac{\tilde{G}(\frac{1}{2}qr, \eta)}{r}. \end{aligned} \quad (2)$$

where $F(\alpha, 1, z)$ is the confluent hypergeometric function, and $\tilde{G}(\frac{1}{2}qr, \eta)$ combines Coulomb functions G_0 and F_0 ,

$$\tilde{G}(\frac{1}{2}qr, \eta) = \sqrt{A_c(\eta)} (G_0(\frac{1}{2}qr, \eta) + iF_0(\frac{1}{2}qr, \eta)), \quad (3)$$

where $A_c(\eta) = \frac{2\pi\eta}{e^{2\pi\eta} - 1}$ with the definition of $\eta = 2/(qa_0)$ (the Bohr radius $a_0 = 57.5\text{fm}$). The S-wave scattering amplitude $f_c(q)$ is expanded as

$$f_c(q) \approx [\frac{1}{f_0} + \frac{1}{8}d_0q^2 - q\eta h(\eta^{-1}) - i\frac{1}{2}qA_c(\eta)]^{-1}, \quad (4)$$

with $h(x = \eta^{-1}) = \sum_{n=1}^{\infty} \frac{1}{n[(nx)^2 + 1]} - C + \ln x$, where $C \approx 0.5772$ is the Euler constant. For identical particles, only considering S-wave, Eq. (1) can be written as following,

$$C(\mathbf{q}) = \int d^3r W_d(\mathbf{q}, \mathbf{r}') S(\mathbf{r}), \quad (5)$$

where $W_d(\mathbf{q}, \mathbf{r}') = \frac{1}{2}[\frac{1}{4}|\psi_{\mathbf{q}}^s(\mathbf{r}') + \psi_{\mathbf{q}}^s(-\mathbf{r}')|^2 + \frac{3}{4}|\psi_{\mathbf{q}}^t(\mathbf{r}') - \psi_{\mathbf{q}}^t(-\mathbf{r}')|^2]$.

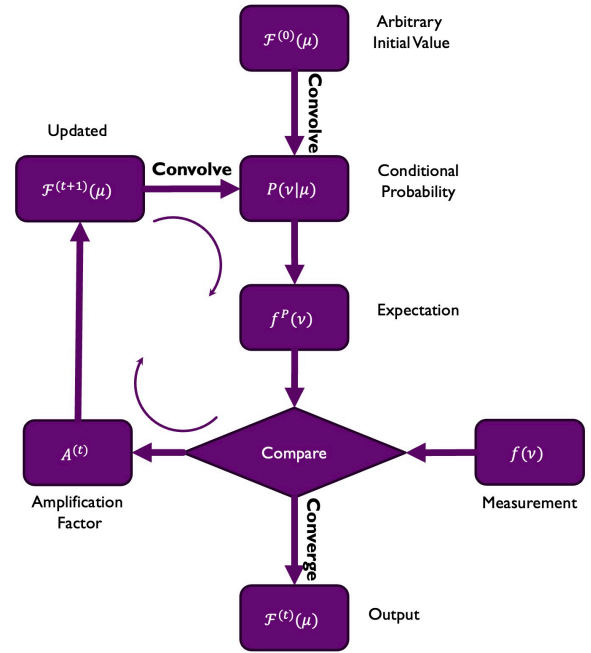


FIG. 1: Diagram of RL algorithm process.

In optical deblurring, the measured distribution $f(\nu)$ can be related to the true photon distribution $\mathcal{F}(\mu)$ using a conditional probability $P(\nu|\mu)$,

$$f(\nu) = \int P(\nu|\mu) \mathcal{F}(\mu) d\mu \quad (6)$$

where the response function $P(\nu|\mu)$ represents the conditional probability that a photon with the true property μ is measured as ν . Although the true distribution $\mathcal{F}(\mu)$ is unknown, it can be inferred from the measured distribution $f(\nu)$ through iterative regression starting from an arbitrary initial guess. This iterative process is illustrated in Fig. 1. Starting with $t = 0$, the arbitrary initial trial $\mathcal{F}^{(0)}(\mu)$ is convolved with $P(\nu|\mu)$ to predict the measurement distribution $f^P(\nu)$, which is then compared to the known measurement distribution $f(\nu)$. Based on the difference between them, an amplification factor $A^{(t)}$ is calculated at each t^{th} iteration. The factor $A^{(t)}$ is functioning to adjust the values of $\mathcal{F}^{(t)}(\mu)$ for the next iteration. Through the iterative process, the updated distribution $\mathcal{F}^{(t+1)}(\mu)$ progressively converges toward the true distribution $\mathcal{F}(\mu)$. The convergence criteria is invoked if $f^P(\nu)$ becomes sufficiently close to $f(\nu)$.

From the mathematical similarity between the KP formula (1) and the optical deblurring equation (6), it is naturally suggested that the RL algorithm can be applied iteratively to solve the SF. By evaluating the converged χ^2 value, one can identify the optimal (f_0, d_0) for the wave function that best describes the CF, thereby achieving both SF imaging and extraction of strong interaction parameters simultaneously. For the convenience of numerical implementation, the KP formula is discretized

by dividing C into N bins and S into M bins ($N \geq M$). The CF C is expressed by S through an $N \times M$ transformation matrix K as

$$C_i = \sum_{j=1}^M K_{ij} S_j. \quad (7)$$

Once the values of C and K are known, the distribution of S can be optimized through the RL algorithm via iterative processes:

$$S_i^{(t+1)} = S_i^{(t)} \frac{\sum_j W_j \frac{C_j}{C_j^{(t)}} K_{ji}}{\sum_{j'} W_{j'} K_{j'i}}, \quad (8)$$

where W represents the weight of the data. According to the measurement errors ϵ of each data point of CFs, the weight W of i^{th} CF point is set to $1/\epsilon_i$ for the iterative process. $C^{(t)}$ is the predicted CF at the t^{th} iteration:

$$C_i^{(t)} = \sum_j K_{ij} S_j^{(t)}. \quad (9)$$

Additionally, it is crucial to consider a moderate number of iterations and an appropriate number of bins to ensure the algorithm's robustness.

The transformation matrix K_{ij} is calculated by

$$K_{ij} = \int_{\text{bin}_j} d\mathbf{Q} |\Psi_{\mathbf{q}_i}(\mathbf{r}')|^2 r^2 \sin\theta dr d\theta d\varphi. \quad (10)$$

where \mathbf{Q} denotes the total momentum of the particle pair in the source rest frame. Here, i and j label the bin indexes of C and S , respectively. In one dimensional imaging, the wave function is assumed to be uniform in the polar θ and azimuthal φ directions, leaving only the r -direction to consider. Consequently, the integration over θ and φ can be performed using Monte Carlo sampling uniformly within the spherical shell. This approach allows for iterative reconstruction of the source distribution from the discretized experimental measurements of C .

For both cases of pp and $\bar{p}\bar{p}$, the transform matrix from Eq. (10) can be written as $K_{ij} = \int_{\text{bin}_j} d\mathbf{Q} W_d(\mathbf{q}_i, \mathbf{r}') r^2 \sin\theta dr d\theta d\varphi$. For each bin of S , the integration of \mathbf{Q} is performed by sampling a large number of particle pairs. Given the momenta \mathbf{p}_1 and \mathbf{p}_2 for each pair in the source rest frame, the relative distance \mathbf{r} is boosted to \mathbf{r}' in the PRF for $W_d(\mathbf{q}_i, \mathbf{r}')$ calculation. It is essential to account for the angles θ and φ . Since only the radial direction r is considered, we assume the particle emission source is isotropic with respect to θ and φ . Thus, θ and φ are sampled uniformly over $\cos\theta$ (from -1 to 1) and φ (from 0 to 2π), and the corresponding integrated values are calculated. The final integrated result for each sampled pair can be calculated using the Monte Carlo integration method which involves averaging over all θ and φ samples, yielding a value independent of these angles. This result is then added to the bin corresponding to the relative momentum in the PRF. After

sampling a large number of particle pairs for each bin of S , the sum in each bin of K_{ij} is divided by the number of sampled pair integrations contributing to it.

III. METHOD TEST

The imaging of the source and the extraction of interaction parameters (f_0, d_0) can now be achieved simultaneously using this method. To test the algorithm, we start with a CF calculated from the given source distribution and known pp interactions. The known source function is modeled as a 1D Gaussian distribution with a mean of 0 and a standard deviation of $\sigma = 3.5$ fm in the radial direction, as illustrated by blue solid curve in Fig. 2 (b). For imaging purposes, the source function is uniformly divided into $M = 20$ bins with a width of 1 fm over the range of 0 to 20 fm in the radial direction, while the CF is divided into $N = 50$ bins with a width of 4 MeV over the range of 0 to 200 MeV. The transformation matrix is calculated using the LL model, incorporating Coulomb interaction, with the interaction parameters for pp interactions specified as $f_0 = 7.8$ fm and $d_0 = 2.77$ fm. The CF used for imaging is obtained by multiplying the transformation matrix with the source function, incorporating the corresponding error values for each point, as shown by the blue line with the purple error band in Fig. 2 (a). In order to mimic the real measurement, the fluctuation is introduced to each point according to the experimental uncertainty. By treating the value C of each point in the CF as the mean of a Gaussian distribution and the associated error as its standard deviation, we can sample numerous CFs. One of these is randomly selected to serve as the central CF, represented by the symbols of hollow blue circle in Fig. 2 (a).

Each sampled CF is then iteratively solved using the imaging method. Since the exact values of (f_0, d_0) , key parameters of the transformation matrix, are unknown, it is reasonable to generate different matrices by exploring all possible values of (f_0, d_0) . In this study, we consider values of (f_0, d_0) within the range of 0 to 10 fm, with a step size of 0.1 fm. For each sampled CF, we solve it using these matrices and compute the corresponding χ^2 values (NDF = N) which represents for the overall deviation. Here χ^2 is defined as

$$\chi^2 = \sum_i^N \left(\frac{C_i^P - C_i}{\sigma_i} \right)^2, \quad (11)$$

where C_i^P represents the value of the i^{th} point. The matrix that yields the minimum χ^2 is considered the best fit to describe the CF, allowing us to simultaneously determine (f_0, d_0) , and the imaged source function.

The initial source function for the iteration is all assumed to be a Gaussian distribution with $\sigma_0 = 3$ fm. Then the inverse problem is iteratively solved from a initial trial of the SF, which is taken as a Gaussian distribution with $\mu = 0$ center location and arbitrary deviation.

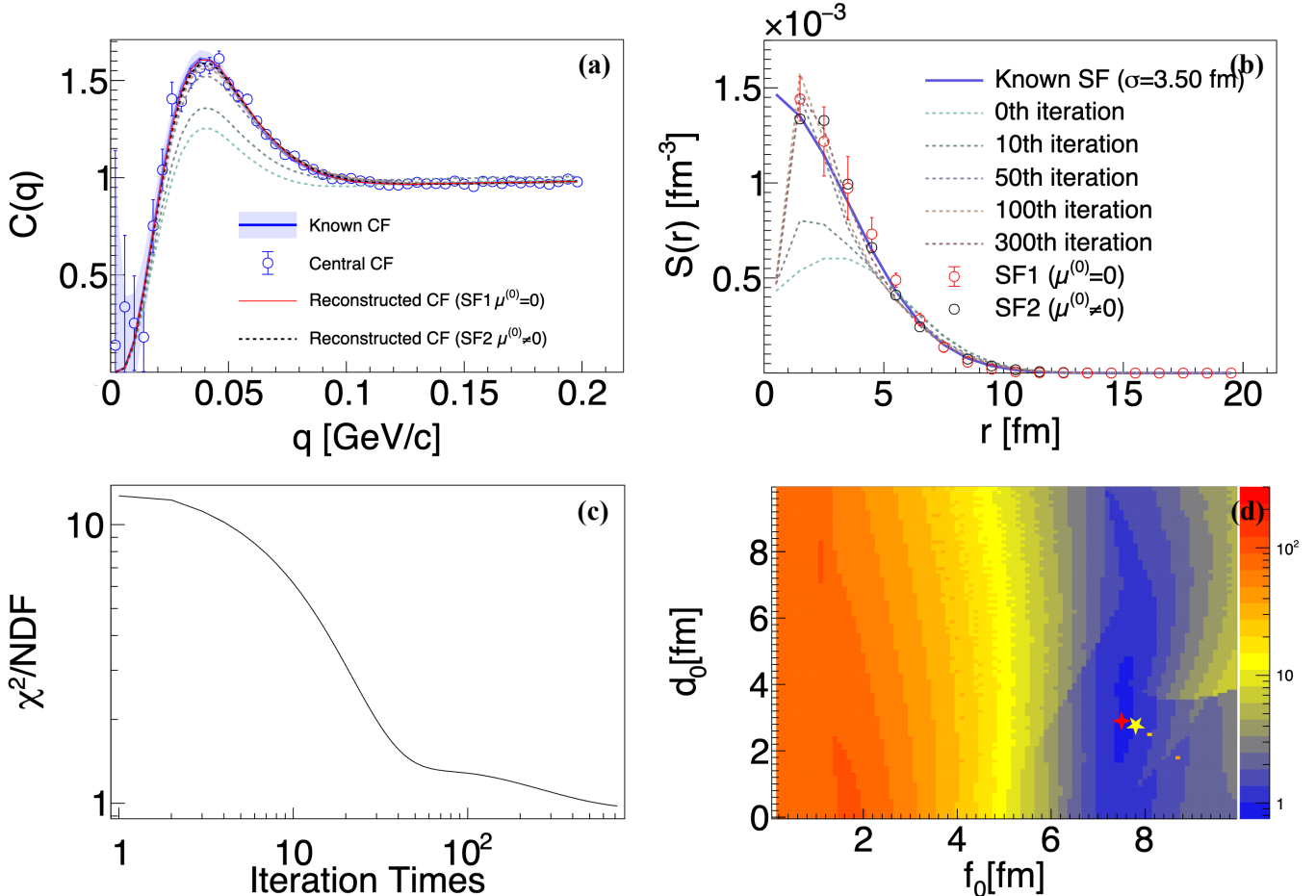


FIG. 2: (Color Online) Model test procedure. (a) The correlations functions. The blue solid curve is the CF calculated using LL model. The symbols are the sampled CF taking into account the uncertainty to mimic the experimental measurement which is selected as the central CF for imaging. The dashed curves are the output at various iteration steps. The red solid and black dashed thin curves are the final reconstructed CF with two different initial trials of the source function SF1 and SF2. (b) The restored source images. The blue solid curve is the given SF to calculate the CF. The red and black symbols are the restored SF at two initial trials SF1 and SF2. (c) The χ^2/NDF as a function of iteration times. (d) The minimum χ^2/NDF on the (f_0, d_0) plane. The yellow star and red cross denote the input value and the final converged solution.

The reconstructed SF ends close to the known one, as marked SF1 in 2 (b). In order to check the robustness of algorithm against the variation of the initial SF, we also test the second initial trial, where the center of the initial Gaussian is arbitrarily set at $\mu = 3$ fm instead of zero peaking. With the iteration going on, the output SF gradually approaches to the known one, as illustrated by the dashed curves in Fig. 2 (b). The marked SF2 sits on top of SF1, evidencing the robustness of the iterative procedure. Fig. 2 (c) presents the closeness quantity χ^2 over iteration times in the imaging process of the central CF. During the procedure, (f_0, d_0) parameters are optimized by minimum χ^2 and the closeness between the output and the known CF is checked in every iteration till the convergence condition is reached, namely the change of χ^2 between two successive iterations is less than 1×10^{-4} , which functions as a threshold to avoid noise amplification.

Fig. 2 (d) shows the minimum χ^2 distribution on the (f_0, d_0) plane. The optimized (f_0, d_0) , marked by red cross, converge to the input one (yellow star). The consistency between the input values and the reconstructed ones in panel (a), (b) and (d) demonstrates the validity of the deblurring algorithm.

Once all sampled CFs have been solved, we can calculate the standard deviations of (f_0, d_0) , and each bin of the imaged source function, which represent the uncertainties in the imaging results. The solution obtained from the selected central CF is considered the central value. The corresponding χ^2 values for different matrices of the central CF are shown in Fig. 2 (d), where the red star marks the optimal (f_0, d_0) . The final solution for (f_0, d_0) is

$$f_0 = (7.5 \pm 0.2) \text{ fm}, d_0 = (2.9 \pm 1.5) \text{ fm}, \quad (12)$$

and the imaged source function is represented by the hollow red circles in Fig. 2 (b). In Fig. 2 (a), the red solid line represent the CF reconstructed using imaging methods. In addition, due to the introduction of a 1 fm cut-off when calculating the Coulomb-inclusive wave function using the LL model, in order to prevent numerical divergence during the solution process, the first point in the source function is unreliable.

IV. APPLICATION TO DATA

Now we apply the method to the pp and $\bar{p}\bar{p}$ CFs in Au+Au at $\sqrt{S_{NN}} = 200$ GeV [29], taken by STAR collaboration [7, 30] at the Relativistic Heavy Ion Collider (RHIC) [31, 32]. The experimental CFs are inclusive and contain the contributions from the residual CFs of $p\Lambda$ and $\Lambda\bar{\Lambda}$. The residual contribution, which shall be subtracted, is derived by the difference between the two fitting curves with and without the feedback corrections shown in [29]. Specifically, the difference between the fitting results of inclusive CFs and $1 + x_{pp(\bar{p}\bar{p})}[C_{pp(\bar{p}\bar{p})} - 1]$ are subtracted based on the experimental data. The relative fraction of protons and antiprotons are estimated by the simulation of THMINATOR2 model under the global DCA cut condition ($DCA < 2cm$). The values of x_{pp} and $x_{\bar{p}\bar{p}}$ are 0.45 and 0.42, respectively. In addition, we suppose that there are no differences between inclusive CF and true $pp(\bar{p}\bar{p})$ CF when $q_{rel} > 160$ MeV, which means we use the experimental data of $q_{rel} > 160$ MeV directly. Subsequently, by combining the values of $x_{pp(\bar{p}\bar{p})}$, the true pp ($\bar{p}\bar{p}$) CFs can be obtained. The pure pp and $\bar{p}\bar{p}$ CFs are presented in Fig. 4 (a) by the symbols, where the uncertainties are taken same as in the experiment for each data point.

In the calculation of the Kernel K_{ij} , one needs the momentum distribution of p and \bar{p} . The transverse momentum p_t distributions are taken from the midrapidity range in the same colliding system [33] measured by PHENIX experiment [34, 35]. The longitudinal rapidity y_1 as well as the azimuth in transverse direction are uniformly distributed. The cuts $0.4 < p_t < 2.5$ GeV/c and $|y_1| < 0.7$ are taken as same as STAR data where the CFs are measured. And then, the three-dimension momentum distributions can be obtained. Specifically, we sample the rapidity uniformly within $-0.7 < y_1 < 0.7$ ($y_1 = \frac{1}{2}\ln(\frac{1+\beta_z}{1-\beta_z})$), the p_t from the distributions reported by the PHENIX experiment satisfied with the cuts of STAR, and the azimuthal angle φ uniformly between 0 and 2π . From these, we obtain the momentum of one particle randomly,

$$p_x = p_t \cos \varphi, p_y = p_t \sin \varphi, p_z = \pm \sqrt{\frac{\beta_z^2(p_t^2 + m_{p(\bar{p})}^2)}{1 - \beta_z^2}}. \quad (13)$$

Based on the momentum sampling method described above, we present the three-dimensional momentum distributions for both protons and antiprotons under the

given conditions. The momentum values required to generate the matrix are then sampled from these distributions.

As well noticed, the LL model provides relatively weak constraints on d_0 when analyzing experimental data. So the widely accepted theoretical and experimental approximation $d_0 = 2.8$ fm is fixed here for both pp and $\bar{p}\bar{p}$ pairs. The convergence criterion is set to 1×10^{-2} . The corresponding optimal values of f_0 obtained are as follows:

$$f_0(pp) = (7.7 \pm 0.2) \text{ fm}, \quad f_0(\bar{p}\bar{p}) = (7.9 \pm 0.3) \text{ fm}, \quad (14)$$

and the corresponding distributions of f_0 are shown in the Fig. 3. The f_0 values for pp and $\bar{p}\bar{p}$ pairs are identical and consistent with both the theoretical calculations and the experimental results from STAR collaboration [7].

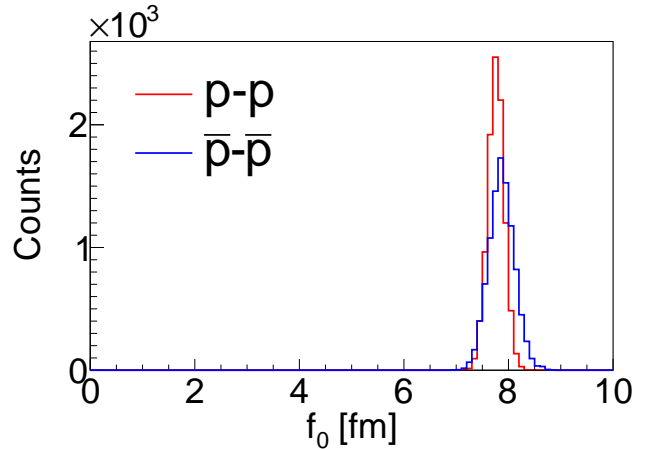


FIG. 3: (Color Online) The distribution of the optimal f_0 values obtained from the imaging of each sampled pseudo-CFs. The red and blue lines represent the optimal f_0 distributions for pp pairs and $\bar{p}\bar{p}$ pairs, respectively.

The converged CFs of pp and $\bar{p}\bar{p}$ reproduce fairly the experimental data, as demonstrated by the solid and dashed curves in Fig. 4 (a), respectively. The results of the restored source imaging are plotted in panel (b) by red dots for p and blue circles for \bar{p} . The red and blue lines are represented for the extracted radii of p and \bar{p} source by STAR, respectively. The extracted radii refer to the single-particle distribution in the source rest frame, which differs from the $S(r)$ defined in this work. In our case, $S(r)$ is a function of the relative distance between two particles. To facilitate comparison, the Gaussian source radii extracted by the STAR collaboration have been multiplied by $\sqrt{2}$. In order to estimate the uncertainty of each imaging point, numerous pseudo-CFs for pp and $\bar{p}\bar{p}$ are sampled, smearing the content in each individual q bin by Gaussian fluctuation, for which the center (standard deviation) is taken from the experimental value (uncertainty). Then the standard deviation of the reconstructed SFs are calculated and plotted on each data point bin-by-bin as the error bar on the SF.

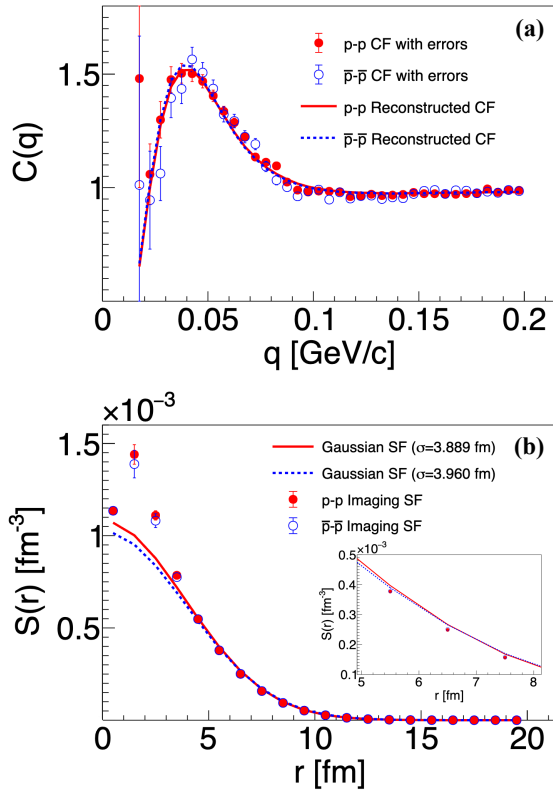


FIG. 4: (Color Online) (a) The reconstructed CFs of pp (red solid curve) and $\bar{p}\bar{p}$ (blue dashed curve) pairs in comparison to the experimental CFs [7] (red dots for pp and blue circles for $\bar{p}\bar{p}$ pairs). (b) Reconstructed SFs for p (red dots) and \bar{p} (blue circles) in Au+Au at center of mass energy 200 GeV. The symbols are the results of direct imaging without Gaussian assumption. The SFs with Gaussian shape obtained in [7] are shown by the curves for reference.

The direct imaging result in Fig. 4 (b) has important implications. First, Within the uncertainty, protons and antiprotons share the identical source distribution at the instant of freeze-out. In addition to the momentum distributions done in [29], the direct imaging result here completes the last piece of evidence of the matter-antimatter symmetry in coordinate space as they are produced and evolve in high energy HICs. This evidence is obtained without imposing assumptions to the shape of the source. Second, the profile of the reconstructed SFs deviates from the Gaussian distribution for both protons and antiprotons. To test whether the imaged source functions for pp and $\bar{p}\bar{p}$ from STAR data are Gaussian distributions, each was fitted with a Gaussian function, and the corresponding chi-square (goodness of fit) values were obtained. For pp and $\bar{p}\bar{p}$, the chi-square values were 91243.5 and 101.078, respectively, with 16 degrees of freedom (19 data points minus 3 parameters in the Gaussian fit). According to the chi-square test, quantitative calculation yields the probabilities for the

SFs to be Gaussian is 0 and 2.2×10^{-14} for p and \bar{p} , respectively. Thus, the Gaussian distribution hypothesis can be excluded. For a clear comparison, the Gaussian distribution obtained in [29] are shown by the curves in panel (b), respectively. It is evident that the emission source are more populated at smaller radius ($r < 5$ fm) but less distributed at larger radius ($5 < r < 8$ fm), as zoomed in in the inset. It is consistent with the picture of an extremely fast collision. Namely, protons and antiprotons, formed by the coalescence of quarks and antiquarks created inside the overlapping region, are not fully randomized in coordinate space prior to the freeze-out instant, otherwise they are expected to extend to the outer space in Gaussian distribution. It offers a support to the recent idea of probing the initial shape of the nucleus via relativistic HIC [13, 36–40], since the collision is so rapid that the spatial information of the colliding nuclei is partially preserved.

The impact of the bin-by-bin variation of the SF on the CF has been analyzed. It is observed that variations in the first few bins of the source function (except for the first bin which is below the low limit cut in LL model calculation) significantly impact the CF, whereas the variations at larger r values are less influential. Inversely, the experimental uncertainty of the CFs near the peak ($q \approx 40$ MeV) brings considerable variation to the SF. In order to achieve more accurate imaging, it is demanded to further reduce the uncertainty of the CF, particularly at small q . If given high-accuracy experimental CFs, the technique developed here offers a novel opportunity to identify exotic nuclear structure on future radioactive ion beam facilities. For instance, one can probe the proton density profile of bubble nucleus which has been recently proposed [41] but yet in debate [42]. Moreover, the imaging method developed in this work is compatible with machine learning techniques, offering a promising avenue for further enhancement and application in nuclear physics research.

V. SUMMARY

A direct imaging method on femtometer scale has been realized by combining the Richardson-Lucy deblurring algorithm and the intensity interferometry in ultra relativistic heavy ion collisions. This method allows for a more accurate extraction of source distributions and final state interaction between particle pair based on the Lednický-Lyuboshitz model analysis. Applying this imaging method to pp and $\bar{p}\bar{p}$ correlation functions in Au+Au at center-of-mass energy 200 GeV measured by the STAR collaboration, we observe the same freeze-out source functions for p and \bar{p} emissions with distinct non-Gaussian characteristics. These findings confirm the matter-antimatter symmetry in coordinate space once produced and suggest the ultrafast feature of the evolution of the collision, which is hardly accessible through other experimental means alone. The new method can

be extended to three dimensional imaging and is inherently compatible with machine learning approaches. It represents a significant advancement of our ability to image the femtoscopic heavy ion collisions and to explore matter-antimatter physics in terrestrial laboratories.

Acknowledgements This work is supported by the National Natural Science Foundation of China under Grant Nos.12335008 and 12205160. The authors acknowledge the support of the Center for High Performance Com-

puting and Initiative Scientific Research Program in Tsinghua University. Sincere gratitude is extended to Xu Nu and Pengfei Zhuang for their valuable suggestions and insightful discussions.

Author contributions JHX, code developing and calculation. ZQ, code reviewing. YJW, analysis and result checking. ZGX, project leading and supervising. All authors contribute to discussions, draft writing and editing.

[1] B. I. Abelev *et al.* (STAR), Observation of an Antimatter Hypernucleus, *Science* **328**, 58 (2010), [arXiv:1003.2030 \[nucl-ex\]](https://arxiv.org/abs/1003.2030).

[2] H. Agakishiev *et al.* (STAR), Observation of the antimatter helium-4 nucleus, *Nature* **473**, 353 (2011), [Erratum: Nature 475, 412 (2011)], [arXiv:1103.3312 \[nucl-ex\]](https://arxiv.org/abs/1103.3312).

[3] M. Abdulhamid *et al.* (STAR), Observation of the antimatter hypernucleus $\Lambda^4\bar{H}$, *Nature* **632**, 1026 (2024), [arXiv:2310.12674 \[nucl-ex\]](https://arxiv.org/abs/2310.12674).

[4] R. Hanbury Brown and R. Q. Twiss, A Test of a new type of stellar interferometer on Sirius, *Nature* **178**, 1046 (1956).

[5] Y. Wang *et al.*, The emission order of hydrogen isotopes via correlation functions in 30 MeV/u Ar+Au reactions, *Phys. Lett. B* **825**, 136856 (2022), [arXiv:2112.02210 \[nucl-ex\]](https://arxiv.org/abs/2112.02210).

[6] Y.-J. Wang *et al.*, CSHINE for studies of HBT correlation in Heavy Ion Reactions, *Nucl. Sci. Tech.* **32**, 4 (2021), [arXiv:2101.07352 \[physics.ins-det\]](https://arxiv.org/abs/2101.07352).

[7] L. Adamczyk *et al.* (STAR), Measurement of Interaction between Antiprotons, *Nature* **527**, 345 (2015), [arXiv:1507.07158 \[nucl-ex\]](https://arxiv.org/abs/1507.07158).

[8] G. Goldhaber, S. Goldhaber, W.-Y. Lee, and A. Pais, Influence of Bose-Einstein statistics on the anti-proton proton annihilation process, *Phys. Rev.* **120**, 300 (1960).

[9] D. H. Boal and J. C. Shillcock, Nuclear interferometry and thermal freeze out, *Phys. Rev. C* **33**, 549 (1986).

[10] D. H. Boal, C. K. Gelbke, and B. K. Jennings, Intensity interferometry in subatomic physics, *Rev. Mod. Phys.* **62**, 553 (1990).

[11] G. Verde, D. A. Brown, P. Danielewicz, C. K. Gelbke, W. G. Lynch, and M. B. Tsang, Imaging sources with fast and slow emission components, *Phys. Rev. C* **65**, 054609 (2002), [arXiv:nucl-ex/0112004](https://arxiv.org/abs/nucl-ex/0112004).

[12] S. Collaboration (STAR), Imaging Shapes of Atomic Nuclei in High-Energy Nuclear Collisions, *Nature* **635**, 67 (2024), [arXiv:2401.06625 \[nucl-ex\]](https://arxiv.org/abs/2401.06625).

[13] S. Zhao, H.-j. Xu, Y. Zhou, Y.-X. Liu, and H. Song, Exploring the nuclear-shape phase transition in ultrarelativistic $^{129}\text{Xe} + ^{129}\text{Xe}$ collisions at the lhc, *Phys. Rev. Lett.* **133**, 192301 (2024).

[14] Z. Wang, J. Zhao, C. Greiner, Z. Xu, and P. Zhuang, Incomplete electromagnetic response of hot QCD matter, *Phys. Rev. C* **105**, L041901 (2022), [arXiv:2110.14302 \[hep-ph\]](https://arxiv.org/abs/2110.14302).

[15] D. A. Brown and P. Danielewicz, Imaging of sources in heavy ion reactions, *Phys. Lett. B* **398**, 252 (1997), [arXiv:nucl-th/9701010](https://arxiv.org/abs/nucl-th/9701010).

[16] P. Chung *et al.*, Comparison of source images for protons, pi's and Lambda's in 6-AGeV Au+Au collisions, *Phys. Rev. Lett.* **91**, 162301 (2003), [arXiv:nucl-ex/0212028](https://arxiv.org/abs/nucl-ex/0212028).

[17] D. A. Brown, A. Enokizono, M. Heffner, R. Soltz, P. Danielewicz, and S. Pratt, Imaging three dimensional two-particle correlations for heavy-ion reaction studies, *Phys. Rev. C* **72**, 054902 (2005), [arXiv:nucl-th/0507015](https://arxiv.org/abs/nucl-th/0507015).

[18] W. H. Richardson, Bayesian-based iterative method of image restoration*, *J. Opt. Soc. Am.* **62**, 55 (1972).

[19] L. B. Lucy, An iterative technique for the rectification of observed distributions, *Astronomical Journal* **79**, 745 (1974).

[20] A. P. Fagun Vankawala, Amit Ganatra, A survey on different image deblurring techniques, *International Journal of Computer Applications* **116**, 15 (2015).

[21] P. Danielewicz and M. Kurata-Nishimura, Deblurring for nuclei: 3d characteristics of heavy-ion collisions, *Phys. Rev. C* **105**, 034608 (2022).

[22] P. Nzabahimana and P. Danielewicz, Source function from two-particle correlation through deblurring, *Physics Letters B* **846**, 138247 (2023).

[23] P. Nzabahimana, T. Redpath, T. Baumann, P. Danielewicz, P. Giuliani, and P. Guèye, Deconvoluting experimental decay energy spectra: The ^{26}O case, *Phys. Rev. C* **107**, 064315 (2023).

[24] J. Vargas, J. Benlliure, and M. Caamaño, Unfolding the response of a zero-degree magnetic spectrometer from measurements of the Δ resonance, *Nuclear Instruments and Methods in Physics Research Section A: Accelerators, Spectrometers, Detectors and Associated Equipment* **707**, 16 (2013).

[25] J. Xu, Y. Qin, Z. Qin, D. Si, B. Zhang, Y. Wang, Q. Niu, C. Xu, and Z. Xiao, Reconstruction of bremsstrahlung γ -rays spectrum in heavy ion reactions with richardson-lucy algorithm, *Phys. Lett. B* **857**, 139009 (2024).

[26] S. E. Koonin, Proton Pictures of High-Energy Nuclear Collisions, *Phys. Lett. B* **70**, 43 (1977).

[27] S. Pratt, T. Csorgo, and J. Zimanyi, Detailed predictions for two pion correlations in ultrarelativistic heavy ion collisions, *Phys. Rev. C* **42**, 2646 (1990).

[28] R. Lednický and V. L. Lyuboshits, Final State Interaction Effect on Pairing Correlations Between Particles with Small Relative Momenta, *Yad. Fiz.* **35**, 1316 (1981).

[29] Z. Zhang and Y. Ma, Study of Interaction Between Antiprotons, *Nucl. Phys. Rev.* **34**, 296 (2017).

[30] K. H. Ackermann *et al.* (STAR), STAR detector overview, *Nucl. Instrum. Meth. A* **499**, 624 (2003).

[31] M. Harrison, T. Ludlam, and S. Ozaki, RHIC project overview, *Nucl. Instrum. Meth. A* **499**, 235 (2003).

[32] STAR Collaboration, Measurement of Interaction between Antiprotons, HEPData (collection) (2016), <https://doi.org/10.17182/hepdata.71504>.

- [33] PHENIX Collaboration, Identified charged particle spectra and yields in Au + Au collisions at $s(\text{NN})^{**}(1/2) = 200\text{-GeV}$, HEPData (collection) (2022), <https://doi.org/10.17182/hepdata.106657>.
- [34] S. S. Adler et al. (PHENIX), Identified charged particle spectra and yields in Au+Au collisions at $S(\text{NN})^{**1/2} = 200\text{-GeV}$, *Phys. Rev. C* **69**, 034909 (2004), [arXiv:nucl-ex/0307022](https://arxiv.org/abs/nucl-ex/0307022).
- [35] K. Adcox et al. (PHENIX), PHENIX detector overview, *Nucl. Instrum. Meth. A* **499**, 469 (2003).
- [36] J. Jia, G. Giacalone, and C. Zhang, Separating the Impact of Nuclear Skin and Nuclear Deformation in High-Energy Isobar Collisions, *Phys. Rev. Lett.* **131**, 022301 (2023), [arXiv:2206.10449](https://arxiv.org/abs/2206.10449) [nucl-th].
- [37] C. Zhang and J. Jia, Evidence of Quadrupole and Octupole Deformations in Zr96+Zr96 and Ru96+Ru96 Collisions at Ultrarelativistic Energies, *Phys. Rev. Lett.* **128**, 022301 (2022), [arXiv:2109.01631](https://arxiv.org/abs/2109.01631) [nucl-th].
- [38] J. Jia, Shape of atomic nuclei in heavy ion collisions, *Phys. Rev. C* **105**, 014905 (2022), [arXiv:2106.08768](https://arxiv.org/abs/2106.08768) [nucl-th].
- [39] G. Giacalone, J. Jia, and C. Zhang, Impact of Nuclear Deformation on Relativistic Heavy-Ion Collisions: Assessing Consistency in Nuclear Physics across Energy Scales, *Phys. Rev. Lett.* **127**, 242301 (2021), [arXiv:2105.01638](https://arxiv.org/abs/2105.01638) [nucl-th].
- [40] Q. Liu, S. Zhao, H.-j. Xu, and H. Song, Determining the neutron skin thickness by relativistic semi-isobaric collisions, *Phys. Rev. C* **109**, 034912 (2024), [arXiv:2311.01747](https://arxiv.org/abs/2311.01747) [nucl-th].
- [41] A. Mutschler et al., A proton density bubble in the doubly magic ^{34}Si nucleus, *Nature Phys.* **13**, 152 (2017), [arXiv:1707.03583](https://arxiv.org/abs/1707.03583) [nucl-ex].
- [42] J. Chen et al., Evolution of the nuclear spin-orbit splitting explored via the $^{32}\text{Si}(d,p)^{33}\text{Si}$ reaction using SOLARIS, *Phys. Lett. B* **853**, 138678 (2024), [arXiv:2404.05434](https://arxiv.org/abs/2404.05434) [nucl-ex].